1

On the Normalized Hilbert Transform and Its Applications in Remote Sensing

Steven R. Long and Norden E. Huang

CONTENTS

1.1 Introduction

The development of this new approach was motivated by the need to describe nonlinear distorted waves in detail, along with the variations of these signals that occur naturally in nonstationary processes (e.g., ocean waves). As has been often noted, natural physical processes are mostly nonlinear and nonstationary. Yet, there have historically been very few options in the available analysis methods to examine data from such nonlinear and nonstationary processes. The available methods have usually been for either linear but nonstationary, or nonlinear but stationary, and statistically deterministic processes. The need to examine data from nonlinear, nonstationary, and stochastic processes in the natural world is due to the nonlinear processes which require special treatment. The past approach of imposing a linear structure (by assumptions) on the nonlinear system is not adequate. Other than periodicity, the detailed dynamics in the processes from the data also need to be determined. This is needed because one of the typical characteristics of nonlinear processes is its intrawave frequency modulation (FM), which indicates the instantaneous frequency (IF) changes within one oscillation cycle.

In the past, when the analysis was dependent on linear Fourier analysis, there was no means of depicting the frequency changes within one wavelength (the intrawave frequency variation) except by resorting to the concept of harmonics. The term ''bound

harmonics'' was often used in this connection. Thus, the distortions of any nonlinear waveform have often been referred to as ''harmonic distortions.'' The concept of harmonic distortion is a mathematical artifact resulting from imposing a linear structure (through assumptions) on a nonlinear system. The harmonic distortions may thus have mathematical meaning, but there is no physical meaning associated with them, as discussed by Huang et al. [1,2]. For example, in the case of water waves, such harmonic components do not have any of the real physical characteristics of a water wave as it occurs in nature. The physically meaningful way to describe such data should be in terms of its IF, which will reveal the intrawave FMs occurring naturally.

It is reasonable to suggest that any such complicated data should consist of numerous superimposed modes. Therefore, to define only one IF value for any given time is not meaningful (see Ref. [3], for comments on the Wigner–Ville distribution). To fully consider the effects of multicomponent data, a decomposition method should be used to separate the naturally combined components completely and nearly orthogonally. In the case of nonlinear data, the orthogonality condition would need to be relaxed, as discussed by Huang et al. [1]. Initially, Huang et al. [1] proposed the empirical mode decomposition (EMD) approach to produce intrinsic mode functions (IMF), which are both monocomponent and symmetric. This was an important step toward making the application truly practical. With the EMD satisfactorily determined, an important roadblock to truly nonlinear and nonstationary analysis was finally removed. However, the difficulties resulting from the limitations stated by the Bedrosian [4] and Nuttall [5] theorems must also be addressed in connection with this approach. Both limitations have firm theoretical foundations and must be considered; IMFs satisfy only the necessary condition, but not the sufficient condition. To improve the performance of the processing as proposed by Huang et al. [1], the normalized empirical mode decomposition (NEMD) method was developed as a further improvement on the earlier processing methods.

1.2 Review of Processing Advances

1.2.1 The Normalized Empirical Mode Decomposition

The NEMD method was developed to satisfy the specific limitations set by the Bedrosian theorem while also providing a sharper measure of the local error when the quadrature differs from the Hilbert transform (HT) result.

From an example data set of a natural process, all the local maxima of the data are first determined. These local maxima are then connected with a cubic spline curve, which gives the local amplitude of the data, $A(t)$, as shown together in Figure 1.1. The envelope obtained through spline fitting is used to normalize the data by

$$y(t) = \frac{a(t)\cos\theta(t)}{A(t)} = \left(\frac{a(t)}{A(t)}\right)\cos\theta(t). \tag{1.1}$$

Here $A(t)$ represents the cubic spline fit of all the maxima from the example data, and thus $a(t)/A(t)$ should normalize $y(t)$ with all maxima then normalized to unity, as shown in Figure 1.2. As is apparent from Figure 1.2, a small number of the normalized data points can still have an amplitude in excess of unity. This is because the cubic spline is through the maxima only, so that at locations where the amplitudes are changing rapidly, the line representing the envelope spline can pass under some of the data points. These occasional

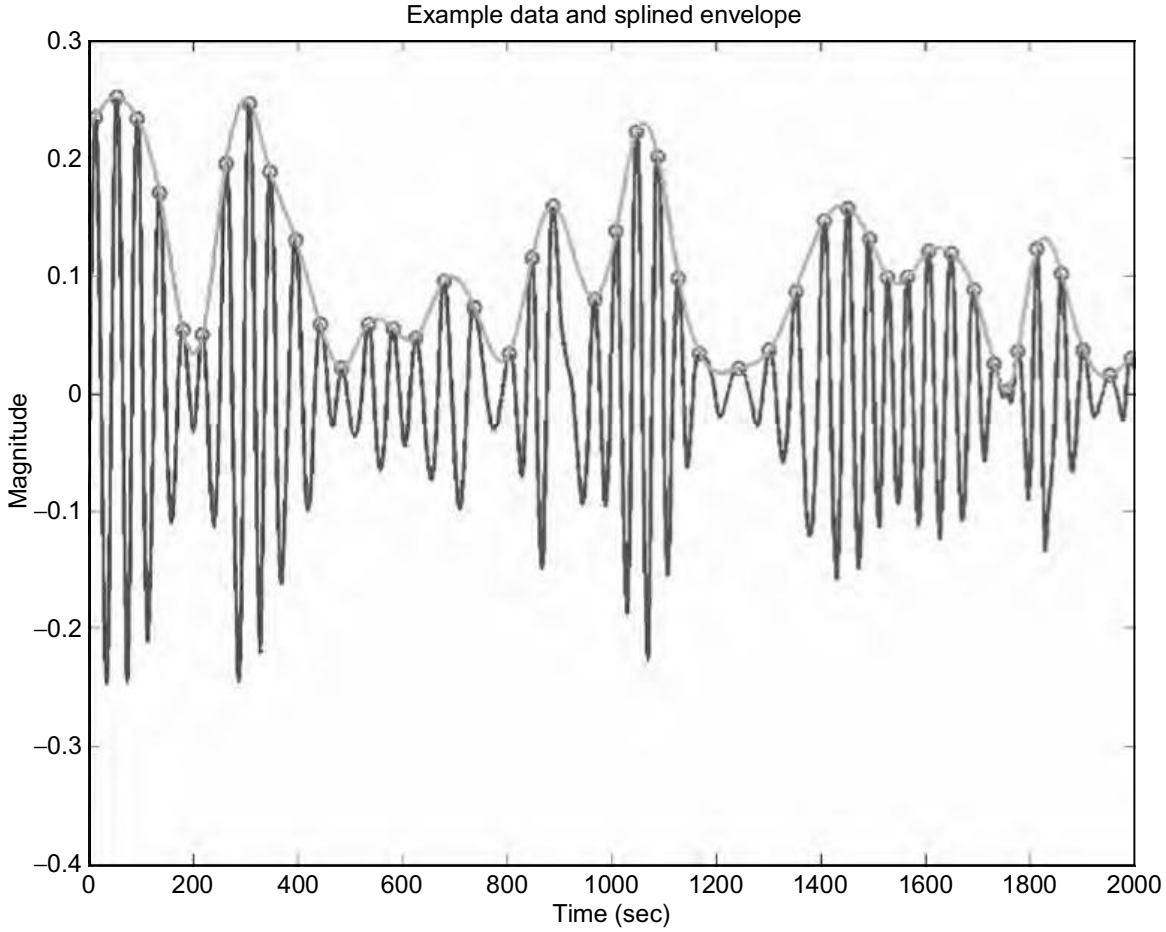

FIGURE 1.1
The best possible cubic spline fit to the local maxima of the example data. The spline fit forms an envelope as an important first step in the process. Note also how the frequency can change within a wavelength, and that the oscillations can occur in groups.

misses are unavoidable, yet the normalization scheme has effectively separated the amplitude from the carrier oscillation. The IF can then be computed from this normalized carrier function $y(t)$, just obtained. Owing to the nearly uniform amplitude, the limitations set by the Bedrosian theorem are effectively satisfied. The IF computed in this way from the normalized data from Figure 1.2 is shown in Figure 1.3, together with the original example data. With the Bedrosian theorem addressed, what of the limitations set by the Nuttall theorem?

If the HT can be considered to be the quadrature, then the absolute value of the HT performed on the perfectly normalized example data should be unity. Then any deviation from the absolute value of the HT from unity would be an indication of a difference between the quadrature and the HT results. An error index can thus be defined simply as

$$E(t) = [\text{abs}(\text{Hilbert transform } (y(t))) - 1]^2. \tag{1.2}$$

This error index would be not only an energy measure as given in the Nuttall theorem but also a function of time as shown in Figure 1.4. Therefore, it gives a local measure of the error resulting from the IF computation. This local measure of error is both logically and practically superior to the integrated error bound established by the Nuttall theorem. If the quadrature and the HT results are identical, then it follows that the error should be

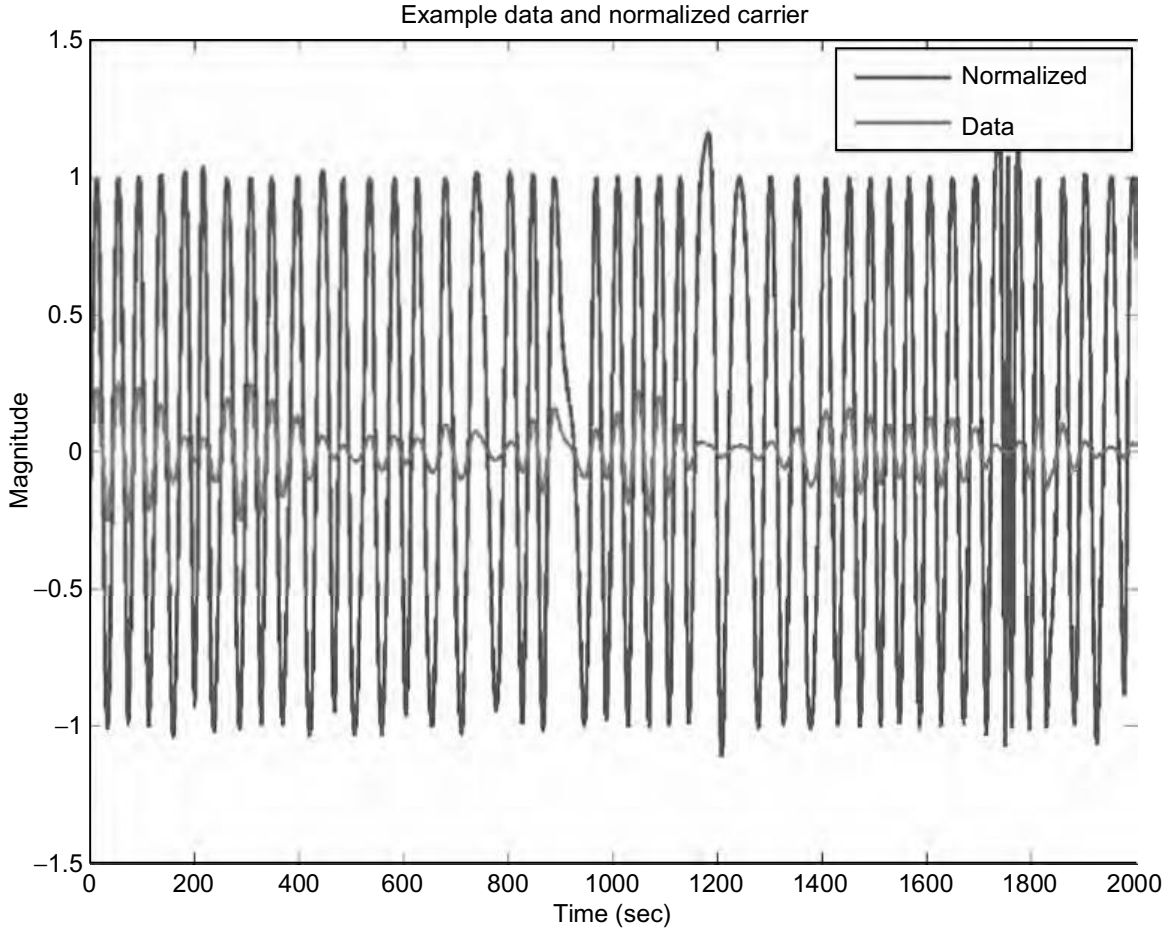

FIGURE 1.2
Normalized example data of Figure 1.1 with the cubic spline envelope. The occasional value beyond unity is due to the spline fit slightly missing the maxima at those locations.

zero. Based on experience with various natural data sets, the majority of the errors encountered here result from two sources. The first source is due to an imperfect normalization occurring at locations close to rapidly changing amplitudes, where the envelope spline-fitting is unable to turn sharply or quickly enough to cover all the data points. This type of error is even more pronounced when the amplitude is also locally small, thus amplifying any errors. The error index from this condition can be extremely large. The second source is due to nonlinear waveform distortions, which will cause corresponding variations of the phase function $\theta(t)$. As discussed by Huang et al. [1], when the phase function is not an elementary function, the differentiation of the phase determined by the HT is not identical to that determined by the quadrature. The error index from this condition is usually small (see Ref. [6]).

Overall, the NEMD method gives a more consistent, stable IF. The occasionally large error index values offer an indication where the method failed simply because the spline misses and cuts through the data momentarily. All such locations occur at the minimum amplitude with a resulting negligible energy density.

1.2.2 Amplitude and Frequency Representations

In the initial methods [1,2,6], the main result of Hilbert spectral analysis (HSA) always emphasized the FM. In the original methods, the data were first decomposed into IMFs, as

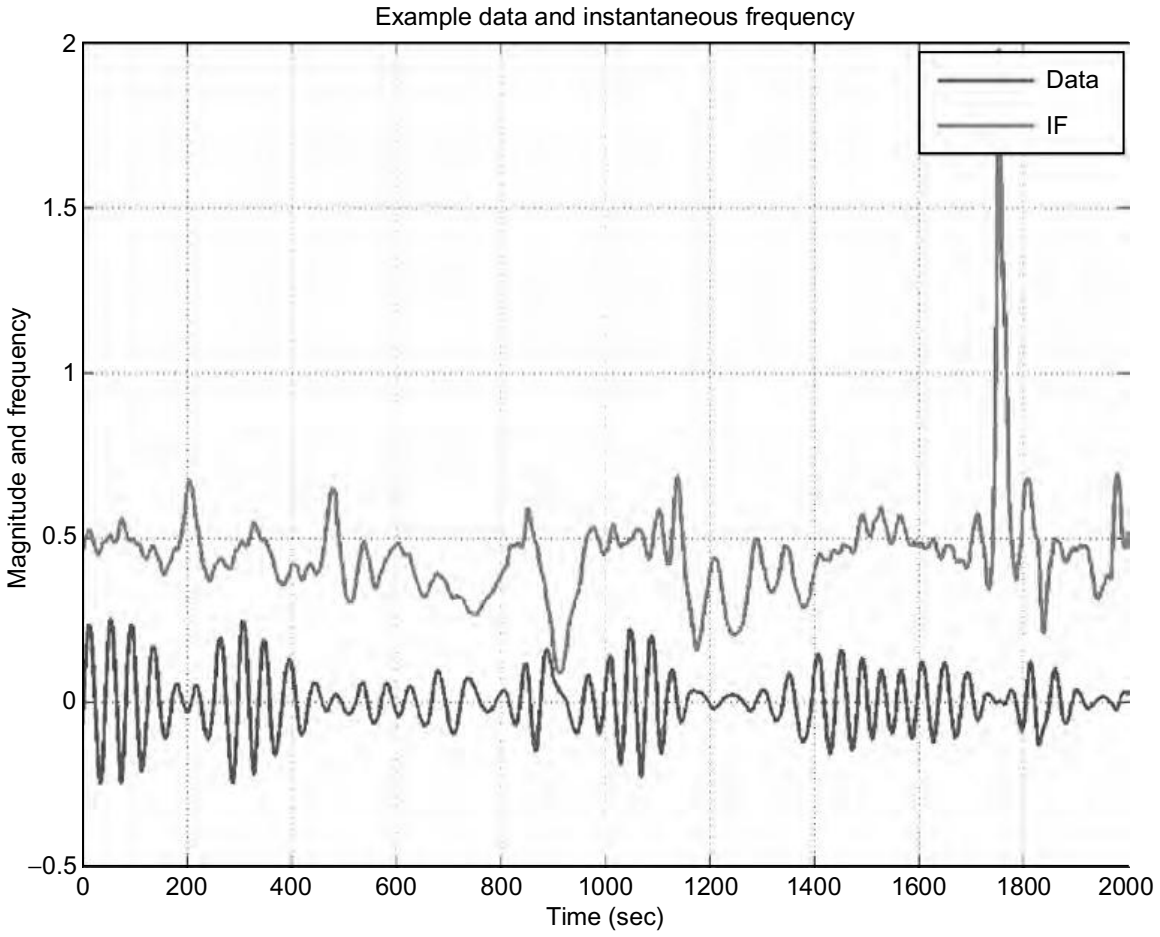

FIGURE 1.3
The instantaneous frequency determined from the normalized carrier function is shown with the example data. Data is about zero, and the instantaneous frequency varies about the horizontal 0.5 value.

defined in the initial work. Then, through the HT, the IF and the amplitude of each IMF were computed to form the Hilbert spectrum. This continues to be the method, especially when the data are normalized. The information on the amplitude or envelope variation is not examined. In the NEMD and HSA approach, it is justifiable not to pay too much attention to the amplitude variations. This is because if there is a mode mixing, the amplitude variation from such mixed mode IMFs does not reveal any true underlying physical processes. However, there are cases when the envelope variation does contain critical information. An example of this is when there is no mode mixing in any given IMF, when a beating signal representing the sum of two coexisting sinusoidal ones is encountered. In an earlier paper, Huang et al. [1] attempted to extract individual components out of the sum of two linear trigonometric functions such as

$$x(t) = \cos at + \cos bt. \tag{1.3}$$

Two seemingly separate components were recovered after over 3000 sifting steps. Yet the obtained IMFs were not purely trigonometric functions anymore, and there were obvious aliases in the resulting IMF components as well as in the residue. The approach proposed then was unnecessary and unsatisfactory. The problem, in fact, has a much simpler solution: treating the envelope as an amplitude modulation (AM), and then processing just the envelope data. The function $x(t)$, as given in Equation 1.3, can then be rewritten as

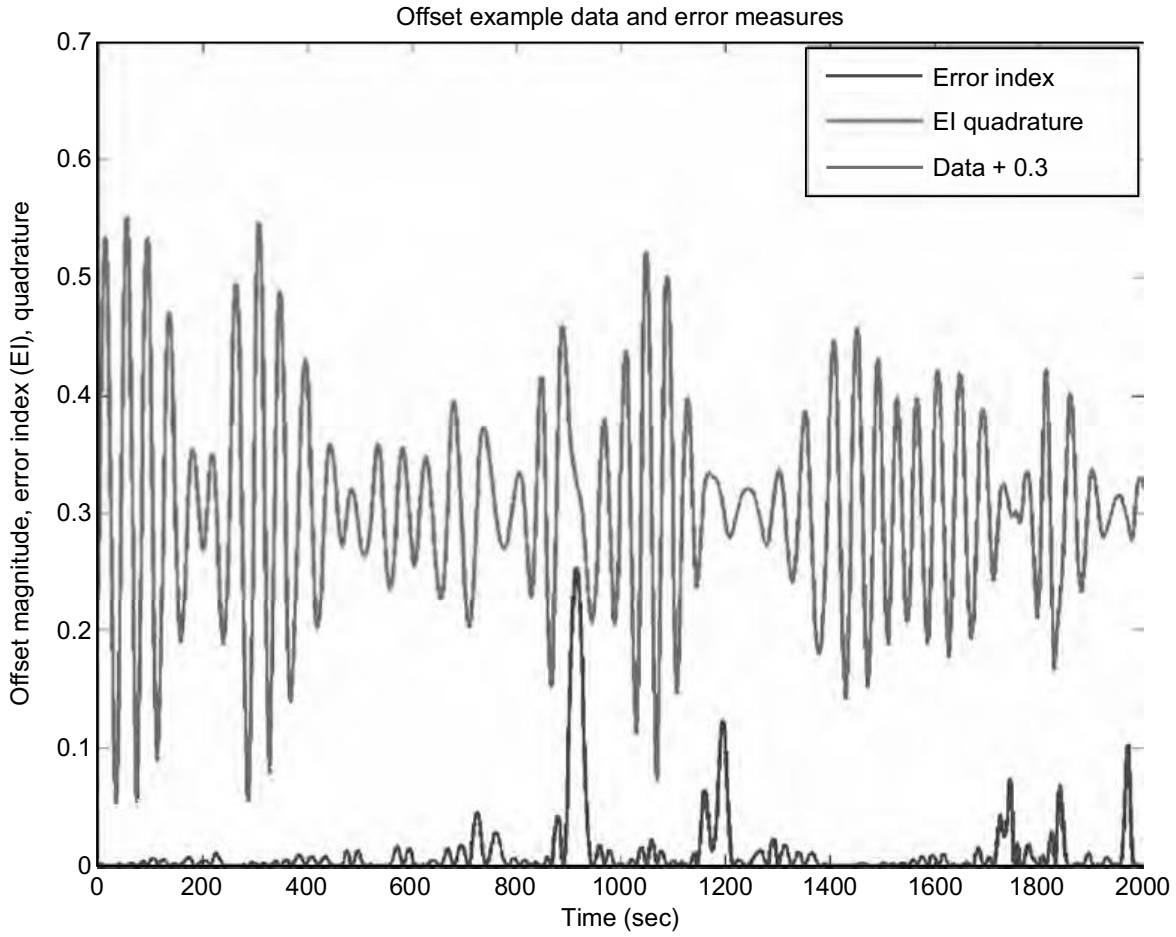

FIGURE 1.4
The error index as it changes with the data location in time. The original example data offset by 0.3 vertically for clarity is also shown. The quadrature result is not visible on this scale.

$$x(t) = \cos at + \cos bt = 2\cos\left(\frac{a+b}{2}t\right)\cos\left(\frac{a-b}{2}t\right). \tag{1.4}$$

There is no difference between the sum of the individual components and the modulating envelope form; they are trigonometric identities. If both the frequency of the carrier wave, $(a+b)/2$, and the frequency of the envelope, $(a-b)/2$, can be obtained, then all the information in the signal can be extracted. This indicates the reason to look for a new approach to extracting additional information from the envelope. In this example, however, the envelope becomes a rectified cosine wave. The frequency would be easier to determine from the simple period counting than from the Hilbert spectral result. For a more general case when the amplitudes of the two sinusoidal functions are not equal, the modulation is not simple anymore. For even more complicated cases, when there are more than two coexisting sinusoidal components with different amplitudes and frequencies, there is no general expression for the envelope and carrier. The final result could be represented as more than one frequency-modulated band in the Hilbert spectrum. It is then impossible to describe the individual components under this situation. In such cases, representing the signal as a carrier and envelope, variation should still be meaningful, for

the dual representations of frequency arise from the different definitions of frequency. The Hilbert-inspired view of amplitude and FMs still renders a correct representation of the signal, but this view is very different from that of Fourier analysis. In such cases, if one is sure of the stationarity and regularity of the signal, Fourier analysis could be used, which will give more familiar results as suggested by Huang et al. [1]. The judgment for these cases is not on which one is correct, as both are correct; rather, it is on which one is more familiar and more revealing.

When more complicated data are present, such as in the case of radar returns, tsunami wave records, earthquake data, speech signals, and so on (representing a frequency ''chirp''), the amplitude variation information can be found by processing the envelope and treating the data as an approximate carrier. When the envelope of frequency chirp data, such as the example given in Figure 1.5, is decomposed through the NEMD process, the IMF components are obtained as shown in Figure 1.6. Using these components (or IMFs), the Hilbert spectrum can be constructed as given in Figure 1.7, together with its FM counterpart. The physical meaning of the AM spectrum is not as clearly defined in this case. However, it serves to illustrate the AM contribution to the variability of the local frequency.

1.2.3 Instantaneous Frequency

It must be emphasized that IF is a very different concept from the frequency content of the data derived from Fourier-based methods, as discussed in great detail by Huang

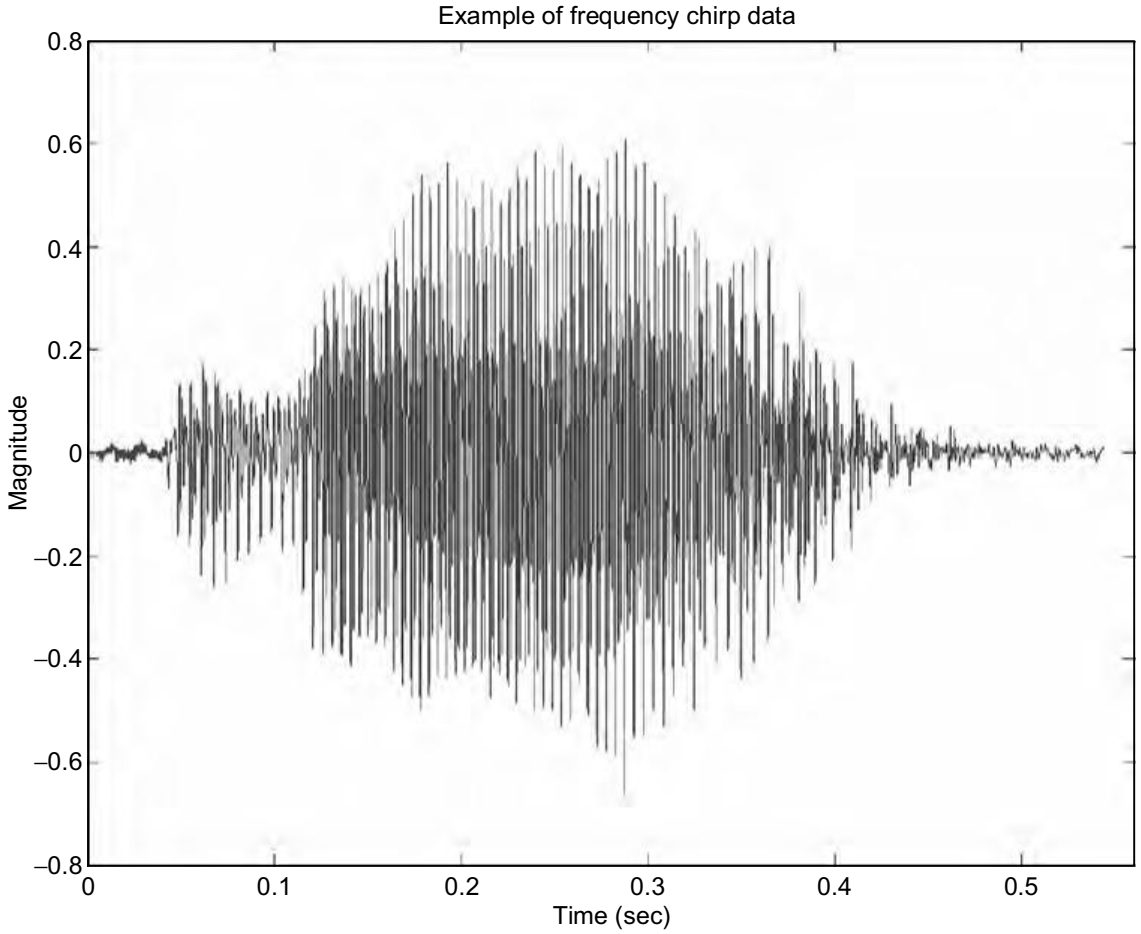

FIGURE 1.5
A typical example of complex natural data, illustrating the concept of frequency ''chirps.''

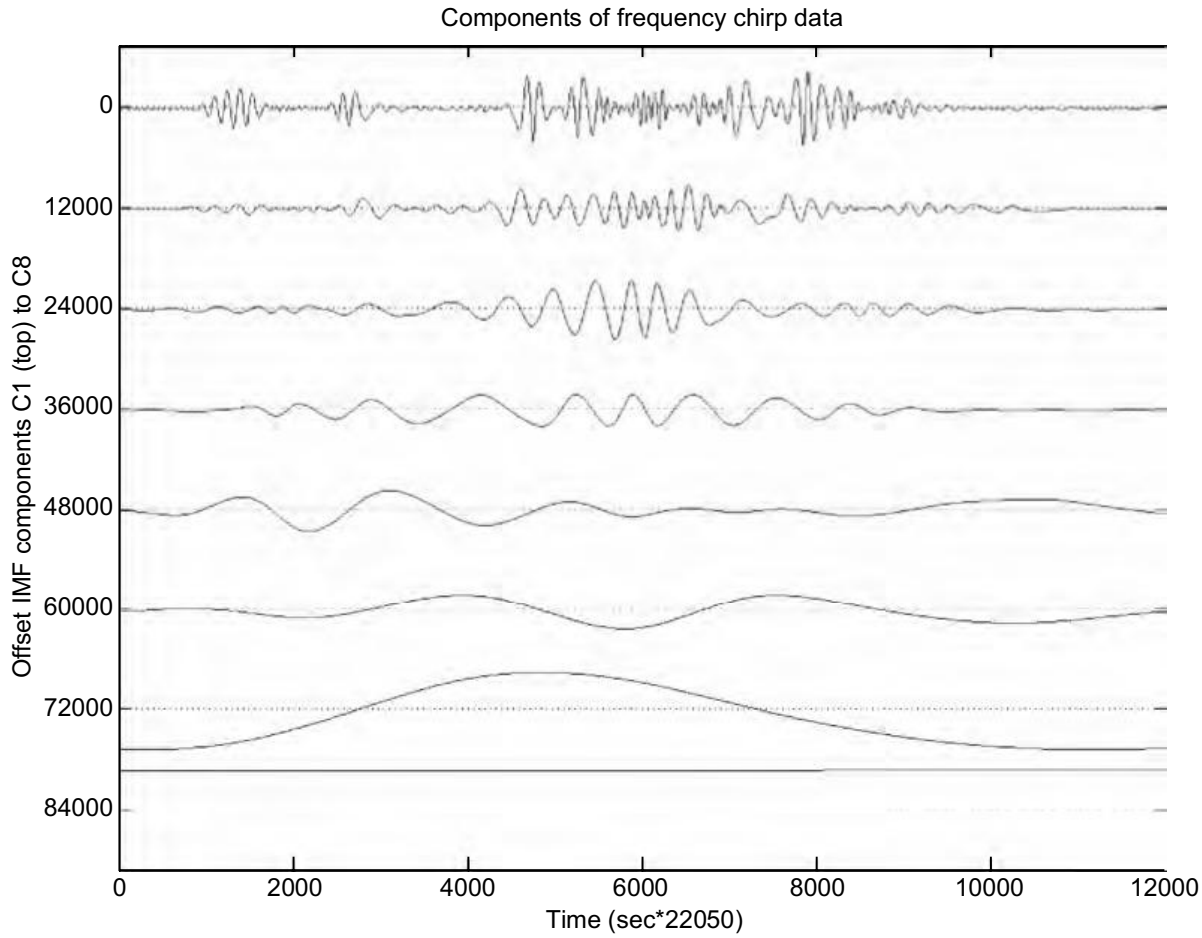

FIGURE 1.6
The eight IMF components obtained by processing the frequency chirp data of Figure 1.5, offset vertically from C1 (top) to C8 (bottom).

et al. [1]. The IF, as discussed here, is based on the instantaneous variation of the phase function from the HT of a data-adaptive decomposition, while the frequency content in the Fourier approach is an averaged frequency on the basis of a convolution of data with an *a priori* basis. Therefore, whenever the basis changes, the frequency content also changes. Similarly, when the decomposition changes, the IF also has to change. However, there are still persistent and common misconceptions on the IF computed in this manner.

One of the most prevailing misconceptions about IF is that, for any data with a discrete line spectrum, IF can be a continuous function. A variation of this misconception is that IF can give frequency values that are not one of the discrete spectral lines. This dilemma can be resolved easily. In the nonlinear cases, when the IF approach treats the harmonic distortions as continuous intrawave FMs, the Fourier-based methods treat the frequency content as discrete harmonic spectral lines. In the case of two or more beating waves, the IF approach treats the data as AM and FM modulation, while the frequency content from the Fourier method treats each constituting wave as a discrete spectral line, if the process is stationary. Although they appear perplexingly different, they represent the same data.

Another misconception is on negative IF values. According to Gabor's [7] approach, the HT is implemented through two Fourier transforms: the first transforms the data into frequency space, while the second performs an inverse Fourier transform after discarding all the negative frequency parts [3]. Therefore, according to this argument, all the negative frequency content has been discarded, which then raises the question, how can there still

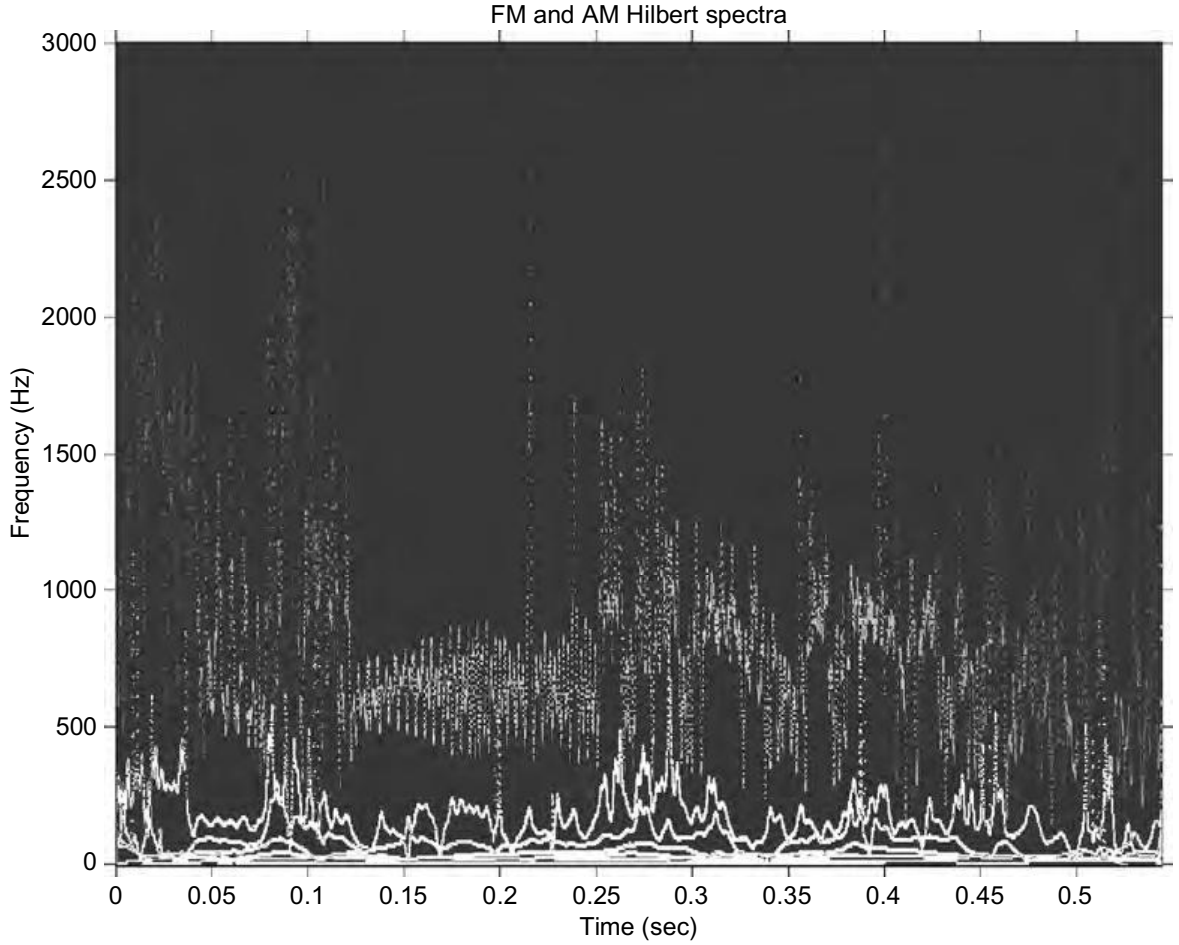

FIGURE 1.7
The AM and FM Hilbert spectral results from the frequency chirp data of Figure 1.5.

be negative frequency values? This question arises due to a misunderstanding of the nature of negative IF from the HT. The direct cause of negative frequency in the HT is the consequence of multiple extrema between two zero-crossings. Then, there are local loops not centered at the origin of the coordinate system, as discussed by Huang et al. [1]. Negative frequency can also occur even if there are no multiple extrema. For example, this would happen when there are large amplitude fluctuations, which cause the Hilbert-transformed phase loop to miss the origin. Therefore, the negative frequency does not influence the frequency content in the process of the HT through Gabor's [7] approach. Both these causes are removed by the NEMD and the normalized Hilbert transform (NHT) methods presented here.

The latest versions of these methods (NEMD/NHT) consistently give more stable IF values. They satisfy the limitation set by the Bedrosian theorem and offer a local measure of error sharper than the Nuttall theorem. Note here that in the initial spline of the amplitude done in the NEMD approach, the end effects again become important. The method used here is just to assign the end points as a maximum equal to the very last value. Other improvements using characteristic waves and linear predictions, as discussed in Ref. [1], can also be employed. There could be some improvement, but the resulting fit will be very similar.

Ever since the introduction of the EMD and HSA by Huang et al. [1,2,8], these methods have attracted increasing attention. Some investigators, however, have expressed certain reservations. For example, Olhede and Walden [9] suggested that the idea of computing

IF through the Hilbert transform is good, but that the EMD approach is not rigorous. Therefore, they have introduced the wavelet projection as the method for decomposition and adopt only the IF computation from the Hilbert transform. Flandrin et al. [10], however, suggest that the EMD is equivalent to a bank of dyadic filters, but refrain from using the HT. From the analysis presented here, it can be concluded that caution when using the HT is fully justified. The limitations imposed by Bedrosian and Nuttall certainly have solid theoretical foundations. The normalization procedure shown here will remove any reservations about further applications of the improved HT methods in data analysis. The method offers relatively little help to the approach advanced by Olhede and Walden [9] because the wavelet decomposition definitely removes the nonlinear distortions from the waveform. The consequence of this, however, is that their approach should also be limited to nonstationary, but linear, processes. It only serves the limited purpose of improving the poor frequency resolution of the continuous wavelet analysis.

As clearly shown in Equation 1.1, to give a good representation of actual wave data or other data from natural processes by means of an analytical wave profile, the analytical profile will need to have IMFs, and also obey the limitations imposed by the Bedrosian and Nuttall theorems. In the past, such a thorough examination of the data has not been done. As reported by Huang et al. [2,8], most of the actual wave data recorded are not composed of single components. Consequently, the analytical representation of a given wave profile in the form of Equation 1.1 poses a challenging problem theoretically.

1.3 Application to Image Analysis in Remote Sensing

Just as much of the data from natural phenomena are either nonlinear or nonstationary, or both, so it is also with the data that form images of natural processes. The methods of image processing are already well advanced, as can be seen in reviews such as by Castleman [11] or Russ [12]. The NEMD/NHT methods can now be added to the available tools for producing new and unique image products. Nunes et al. [13] and Linderhed [14–16], among others, have already done significant work in this new area. Because of the nonlinear and nonstationary nature of natural processes, the NEMD/NHT approach is especially well suited for image data, giving frequencies, inverse distances, or wave numbers as a function of time or distance, along with the amplitudes or energy values associated with these, as well as a sharp identification of imbedded structures. The various possibilities and products of this new analysis approach include, but are not limited to, joint and marginal distributions, which can be viewed as isosurfaces, contour plots, and surfaces that contain information on frequency, inverse wavelength, amplitude, energy and location in time, space, or both. Additionally, the concept of component images representing the intrinsic scales and structures imbedded in the data is now possible, along with a technique for obtaining frequency variations of structures within the images.

The laboratory used for producing the nonlinear waves, used as an example here, is the NASA Air–Sea Interaction Research Facility (NASIRF) located at the NASA Goddard Space Flight Center/Wallops Flight Facility, at Wallops Island, Virginia, within the Ocean Sciences Branch. The test section of the main wave tank is 18.3 m long and 0.9 m wide, filled to a depth of 0.76 m of water, leaving a height of 0.45 m over the water for airflow,

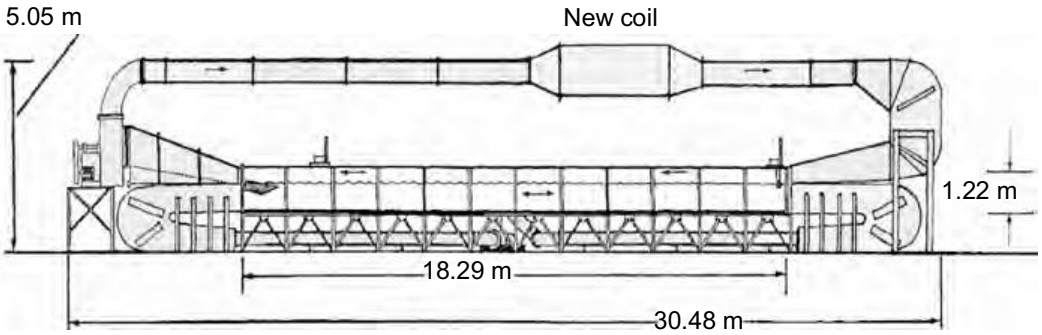

FIGURE 1.8
The NASA Air–Sea Interaction Research Facility's (NASIRF) main wave tank at Wallops Island, VA. The new coils shown were used to provide cooling and humidity control in the airflow overheated water.

if needed. The facility can produce wind and paddle-generated waves over a water current in either direction, and its capabilities, instruments and software have been described in detail by Long and colleagues [17–21]. The basic description is shown with an additional new feature indicated as *new coil* in Figure 1.8. These were recently installed to provide cold air of controlled temperature and humidity for experiments using cold air overheated water during the Flux Exchange Dynamics Study of 2004 (FEDS4) experiments, a joint experiment involving the University of Washington/Applied Physics Laboratory (UW/APL), The University of Alberta, the Lamont-Doherty Earth Observatory of Columbia University, and NASA GSFC/Wallops Flight Facility. The cold airflow overheated water optimized conditions for the collection of infrared (IR) video images.

1.3.1 The IR Digital Camera and Setup

The camera used to acquire the laboratory image presented here as an example was provided by UW/APL as part of FEDS4. The experimental setup is shown in Figure 1.9. For the example shown here, the resolution of the IR image was 640 × 512 pixels. The camera was mounted to look upwind at the water surface, so that its pixel image area covered a physical rectangle on the water surface on the order of 10 cm per side. The water within the wave tank was heated by four commercial spa heaters, while the air in the airflow was cooled and humidity controlled by NASIRF's new cooling and reheating coils. This produced a very thin layer of surface water that was cooled, so that whenever wave spilling and breaking occurred, it could be immediately seen by the IR camera.

1.3.2 Experimental IR Images of Surface Processes

With this imaging system in place, steps were taken to acquire interesting images of wave breaking and spilling due to wind and wave interactions. One such image is illustrated in Figure 1.10. To help the eyes visualize the image data, the IR camera intensity levels have been converted to a grey scale.

Using a horizontal line that slices through the central area of the image at the value of 275, Figure 1.11 illustrates the details contained in the actual array of data values obtained from the IR camera. This gives the IR camera intensity values stored in the pixels along the horizontal line. These can then be converted to actual temperatures when needed. A complex structure is evident here. Breaking wave fronts are evident in the crescent-

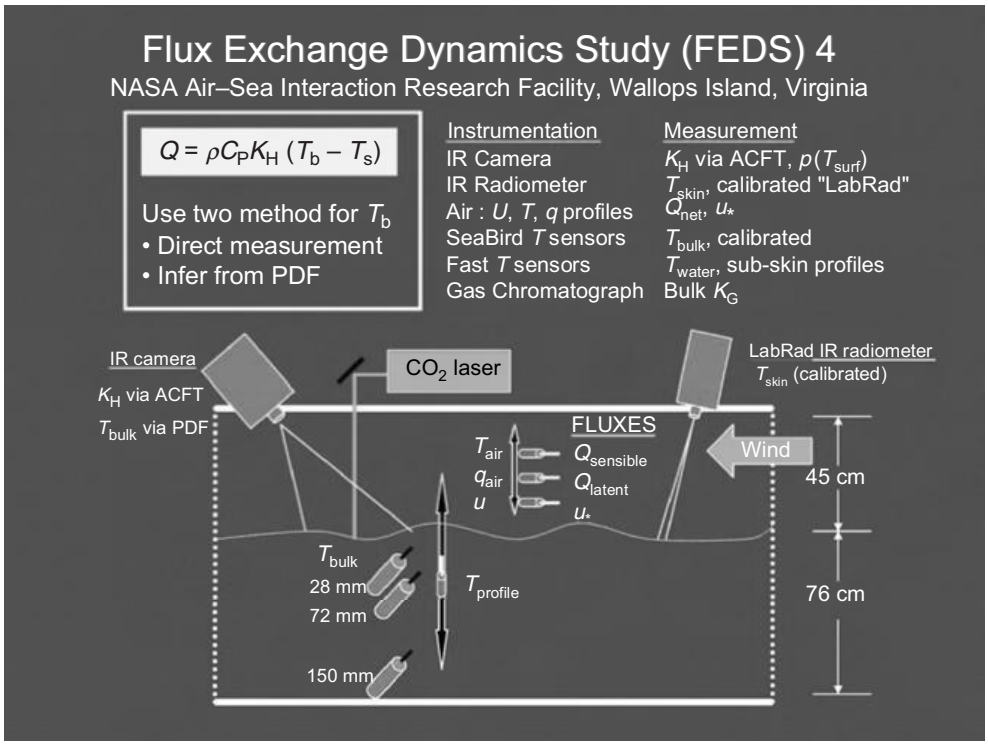

FIGURE 1.9
The experimental arrangement of FEDS4 (Flux Exchange Dynamics Study of 2004) used to capture IR images of surface wave processes. (Courtesy of A. Jessup and K. Phadnis of UW/APL.)

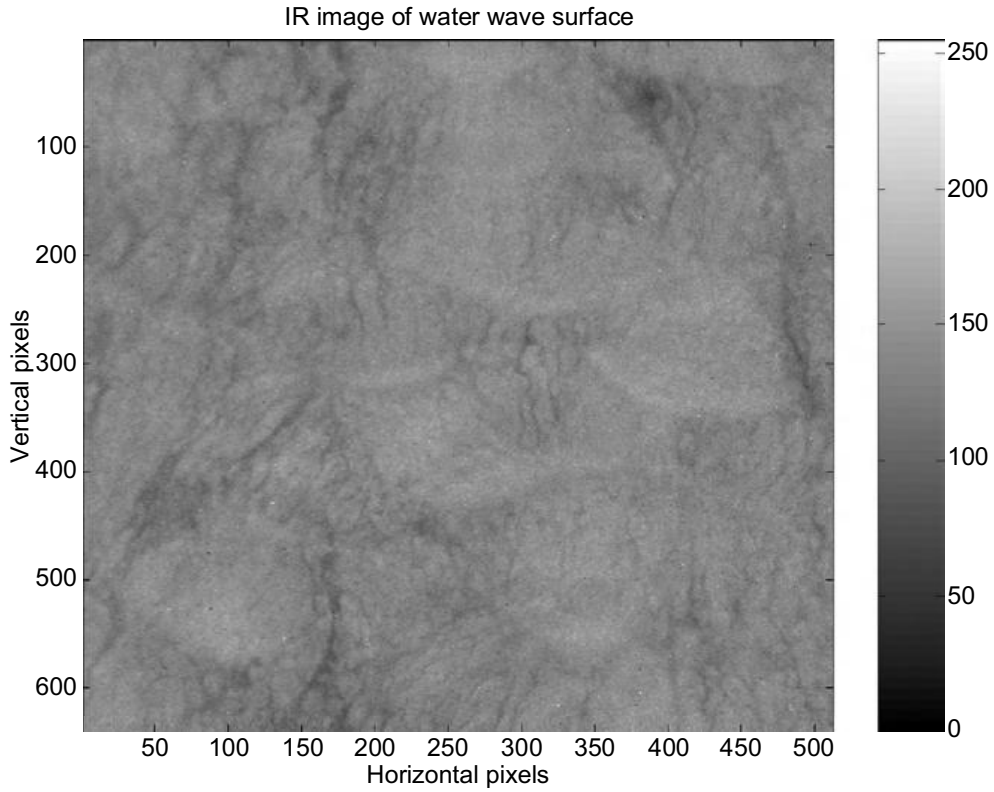

FIGURE 1.10
Surface IR image from the FEDS4 experiment. Grey bar gives the IR camera intensity levels. (Data courtesy of A. Jessup and K. Phadnis of UW/APL.)

shaped structures, where spilling and breaking brings up the underlying warmer water. After processing, the resulting components produced from the horizontal row of Figure 1.11 are shown in Figure 1.12. As can be seen, the component with the longest scale, C9, contains the bulk of the intensity values. The shorter, riding scales are fluctuations about the levels shown in component C9. The sifting was done via the extrema approach discussed in the foundation articles, and produced a total of nine components.

Using this approach, the IR image was first divided into 640 horizontal rows of 512 values each. The rows were then processed to produce the components, each of the 640 rows producing a component set similar to that shown in Figure 1.12. From these basic results, component images can be assembled. This is done by taking the first component representing the shortest scale from each of the 640 component sets. These first components are then assembled together to produce an array that is also 640 rows by 512 columns and can also be visualized as an image. This is the first component image. This production of component images is then continued in a similar fashion with the remaining components representing progressively longer scales. To visualize the shortest component scales, component images 1 through 4 were added together, as shown in Figure 1.13. Throughout the image, streaks of short wavy structures can be seen to line up in the wind direction (along the vertical axis). Even though the image is formed in the IR camera by measuring heat at many different pixel locations over a rectangular area, the surface waves have an effect that can be thus remotely sensed in the image, either as streaks of warmer water exposed by breaking or as more wavelike structures. If the longer scale components are now combined using the 5th and 6th component images, a composite image is obtained as shown in Figure 1.14. Longer scales can be seen throughout the image area where breaking and mixing occur. Other wavelike

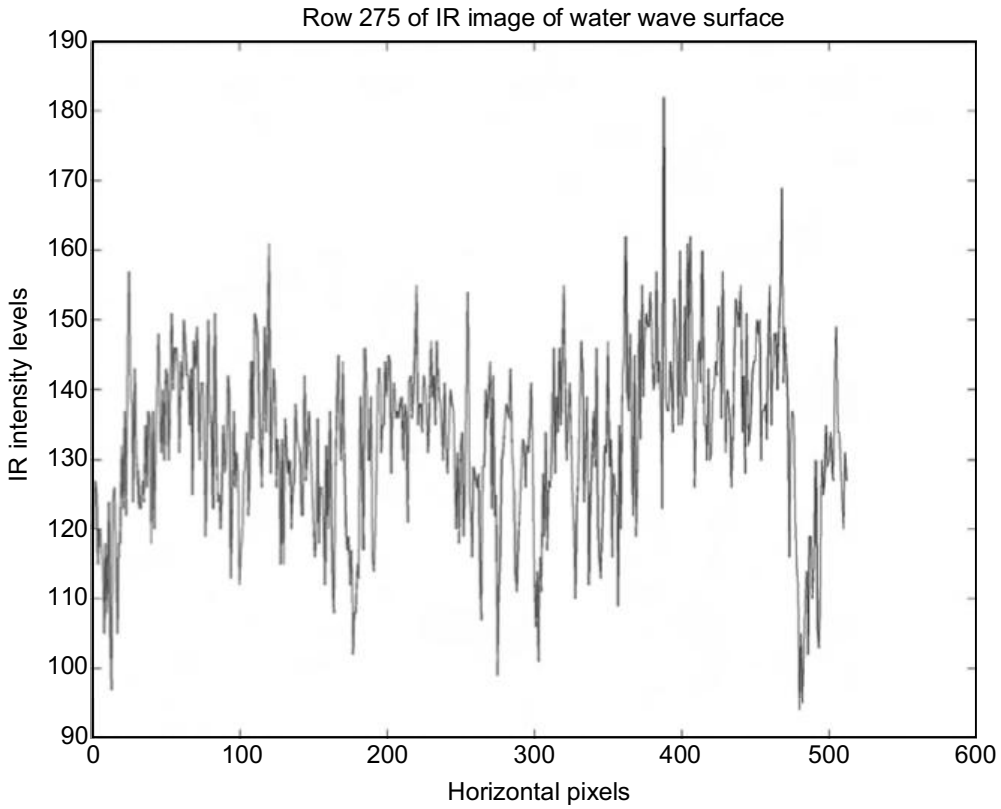

FIGURE 1.11
A horizontal slice of the raw IR image given in Figure 1.10, taken at row 275. Note the details contained in the IR image data, showing structures containing both short and longer length scales.

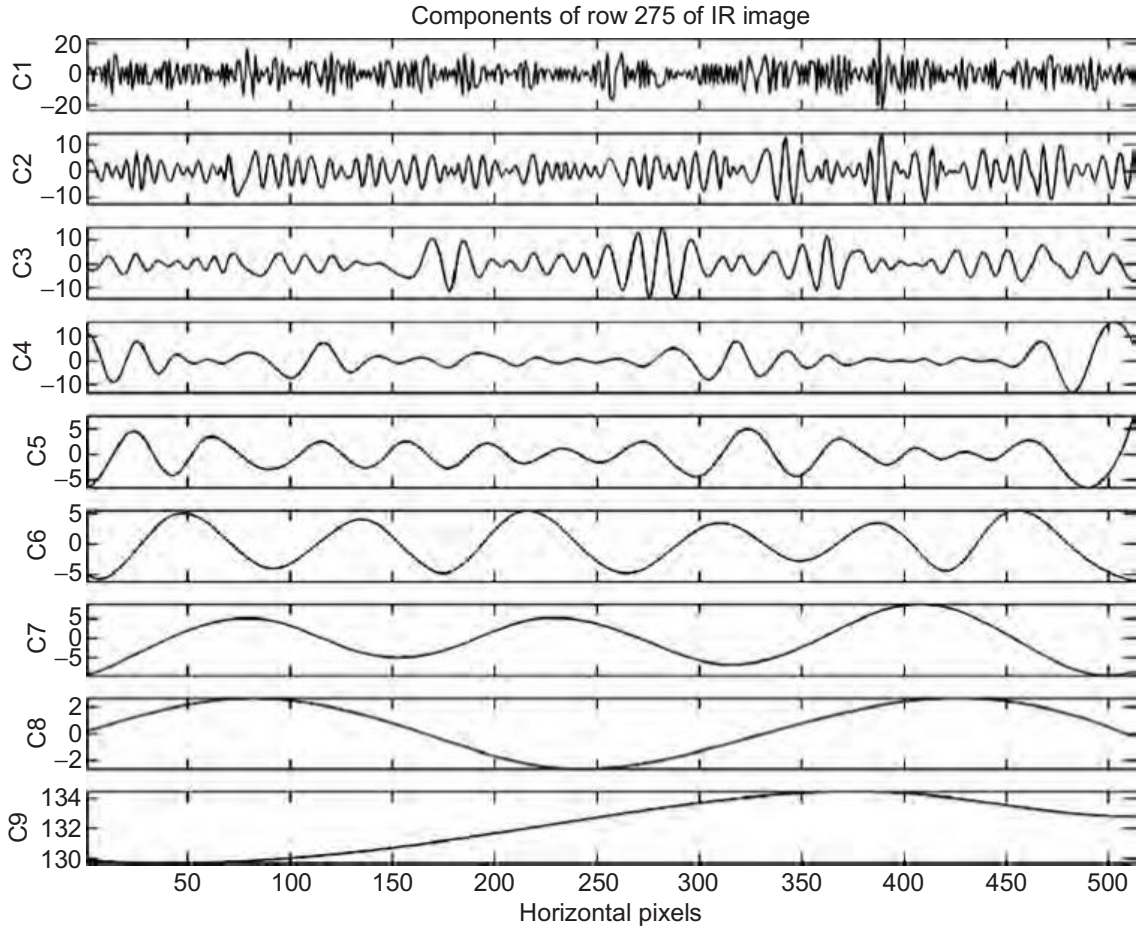

FIGURE 1.12
Components obtained by processing data from the slice shown in Figure 1.11. Note that component C9 carries the bulk of the intensity scale, while the other components with shorter scales record the fluctuations about these base levels.

structures of longer wavelengths are also visible. To produce a true wave number from images like these, one only has to convert using

$$k = 2\pi/\lambda, \tag{1.5}$$

where k is wave number (in 1/cm) and λ is wavelength (in cm). This would only require knowing the physical size of the image in centimeters or some other unit and its equivalent in pixels from the array analyzed.

Another approach to the raw image of Figure 1.10 is to separate the original image into columns instead of rows. This would make the analysis more sensitive to structures that were better aligned with that direction, and also with the direction of wind and waves. By repeating the steps leading to Figure 1.13, the shortest scale component images in component images 3 to 5 can be combined to form Figure 1.15. Component images 1 and 2 developed from the vertical column analysis were not included here, after they were found to contain results of such a short scale uniformly spread throughout the image, and without structure. Indeed, they had the appearance of uniform noise. It is apparent that more structures at these scales can be seen by analyzing along the column direction. Figure 1.16 represents the longer scale in component image 6. By the 6th component image, the lamination process starts to fail somewhat in reassembling the image from the components. Further processing is needed to better match the results at these longer scales.

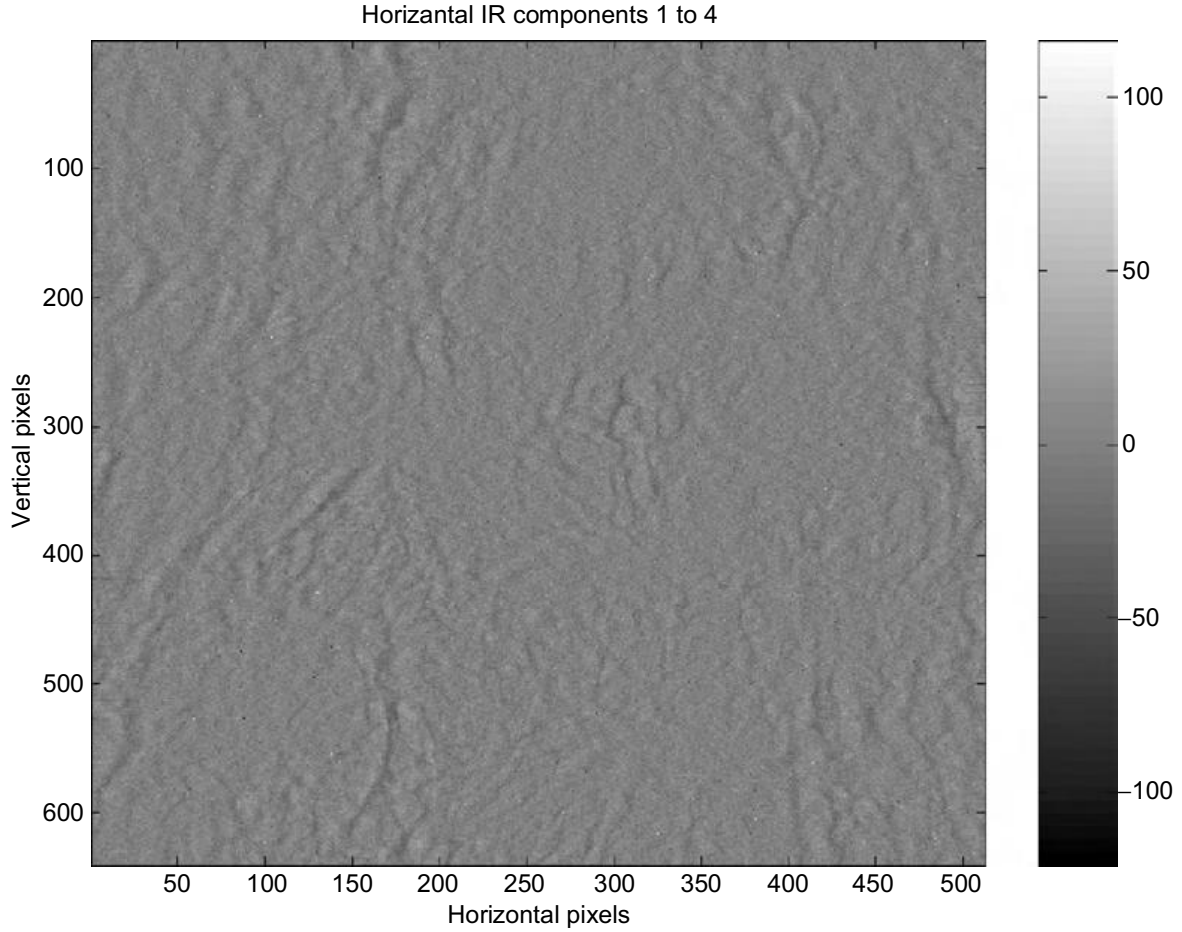

FIGURE 1.13 (See color insert following page 178.)
Component images 1 to 4 from the horizontal rows used to produce a composite image representing the shortest scales.

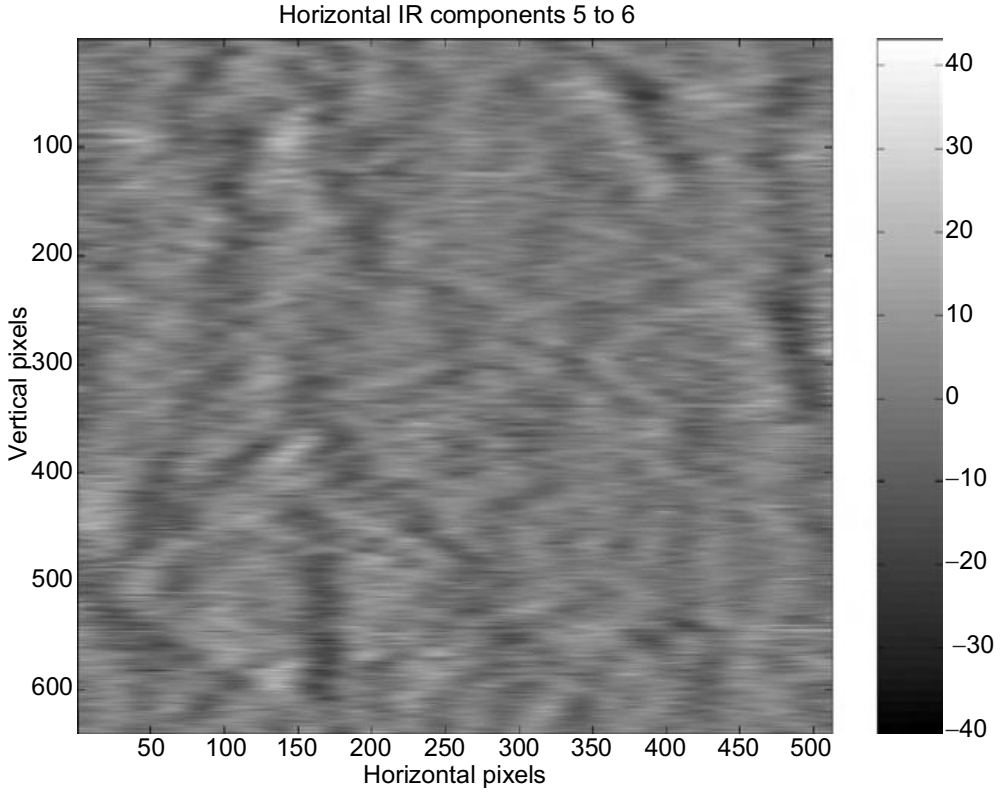

FIGURE 1.14 (See color insert following page 178.)
Component images 5 to 6 from the horizontal rows used to produce a composite image representing the longer scales.

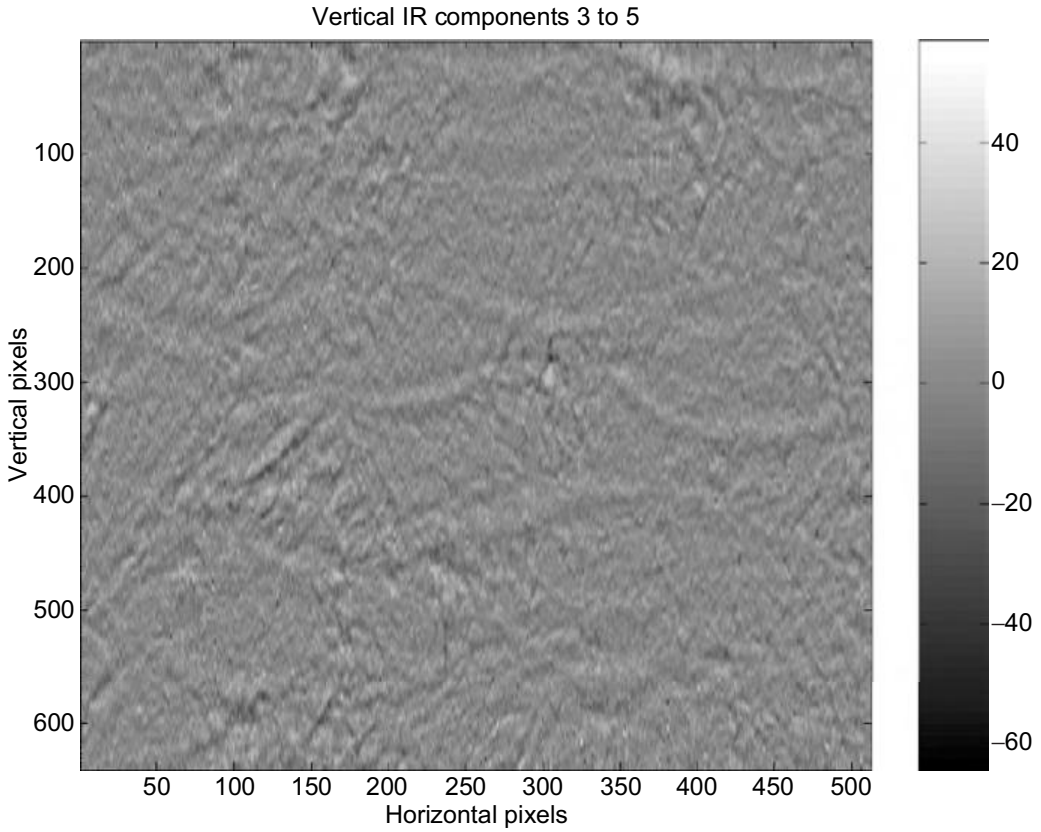

FIGURE 1.15 (See color insert following page 178.)
Component images 3 to 5 from the vertical rows here combined to produce a composite image representing the midrange scales.

When the original data are a function of time, this new approach can produce the IF and amplitude as functions of time. Here, the original data are from an IR image, so that any slice through the image (horizontal or vertical) would be a set of camera values (ultimately temperature) representing the temperature variation over a physical length. Thus, instead of producing frequency (inverse time scale), the new approach here initially produces an inverse length scale. In the case of water surface waves, this is the familiar scale of the wave number, as given in Equation 1.5. To illustrate this, consider Figure 1.17, which shows the changes of scale along the selected horizontal row 400. The largest measures of IR energy can be seen to be at the smaller inverse length scales, which imply that it came from the longer scales of components 3 and 4. Figure 1.18 repeats this for the even longer length scales in components 5 and 6.

Returning to the column-wise processing at column 250 of Figure 1.15 and Figure 1.16, further processing gives the contour plot of Figure 1.19, for components 3 through 5, and Figure 1.20, for components 4 through 6.

1.3.3 Volume Computations and Isosurfaces

Many interesting phenomena happen in the flow of time, and thus it is interesting to note how changes occur with time in the images. To include time in the analysis, a sequence of images taken at uniform time steps can be used.

By starting with a single horizontal or vertical line from the image, a contour plot can be produced, as was shown in Figure 1.7 through Figure 1.20. Using a set of sequential images covering a known time period and a pixel line of data from each (horizontal or vertical), a set of numerical arrays can be obtained from the NEMD/NHT analysis. Each

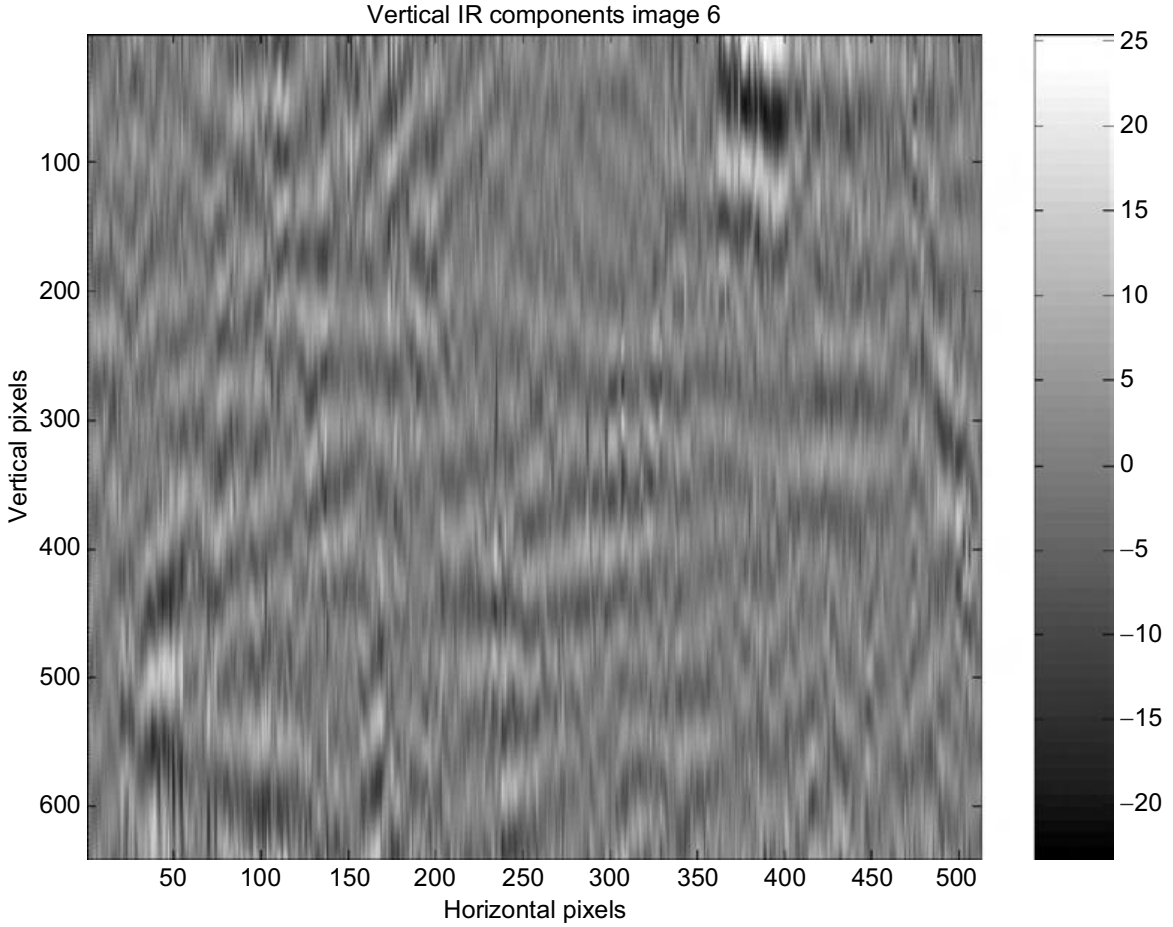

FIGURE 1.16 (See color insert following page 178.)
Component image 6 from the vertical row used to produce a composite image representing the longer scale.

array can be visualized by means of a contour plot, as already shown. The entire set of arrays can also be combined in sequence to form an array volume, or an array of dimension 3. Within the volume, each element of the array contains the amplitude or intensity of the data from the image sequence. The individual element location within the three-dimensional array specifies values associated with the stored data. One axis (call it x) of the volume can represent horizontal or vertical distance down the data line taken from the image. Another axis (call it y) can represent the resulting inverse length scale associated with the data. The additional axis (call it z) is produced by laminating the arrays together, and represents time, because each image was acquired in repetitive time steps. Thus, the position of the element in the volume gives location x along the horizontal or vertical slice, inverse length along the y-axis, and time along the z-axis.

Isosurface techniques would be needed to visualize this. This could be compared to peeling an onion, except that the different layers, or spatial contour values, are not bound in spherical shells. After a value of data intensity is specified, the isosurface visualization makes all array elements transparent outside of the level of the value chosen, while shading in the chosen value so that the elements inside that level (or behind it) cannot be seen. Some examples of this procedure can be seen in Ref. [21].

Another approach with the analysis of images is to reassemble lines from the image data using a different format. A sequence of images in units of time is needed, and using the same horizontal or vertical line from each image in the time sequence, each line can be laminated to its predecessor to build up an array that is the image length along the chosen line along one edge, and the number of images along the other axis, in units of

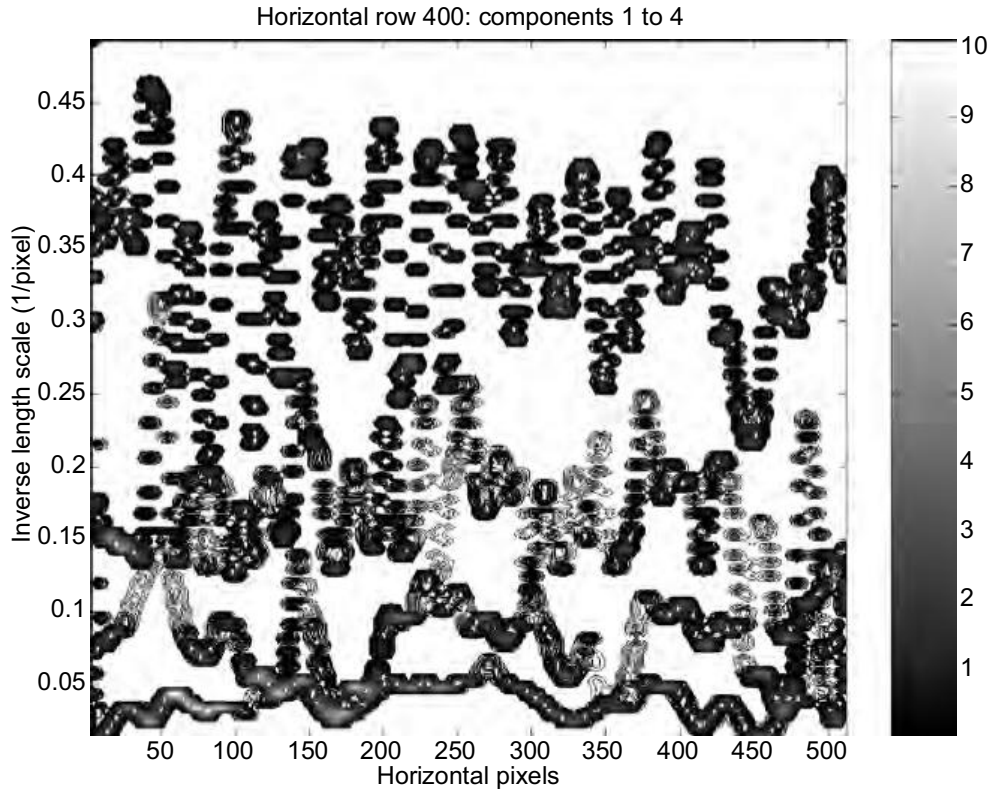

FIGURE 1.17 (See color insert following page 178.)
The results from the NEMD/NHT computation on horizontal row 400 for components 1 to 4, which resulted from Figure 1.13. Note the apparent influence of surface waves on the IR information. The most intense IR radiation can be seen at the smaller values of inverse length scale, denoting the longer scales in components 3 and 4. A wavelike influence can be seen at all scales.

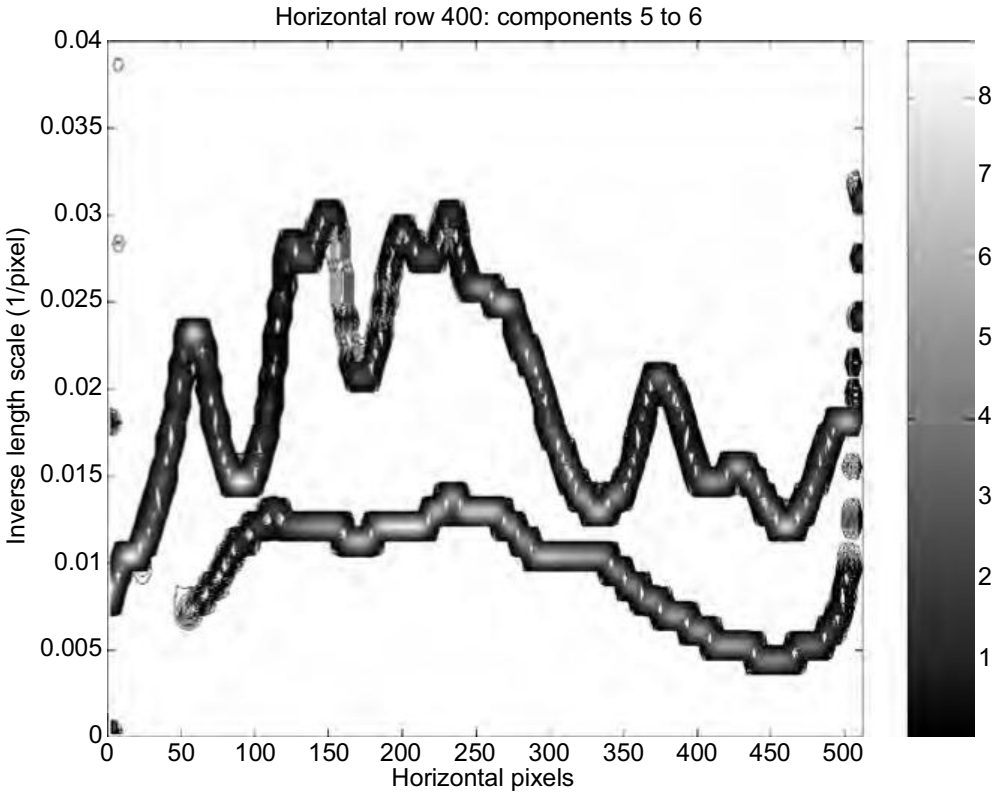

FIGURE 1.18 (See color insert following page 178.)
The results from the NEMD/NHT computation on horizontal row 400 for components 5 to 6, which resulted from Figure 1.14. Even at the longer scales, an apparent influence of surface waves on the IR information can still be seen.

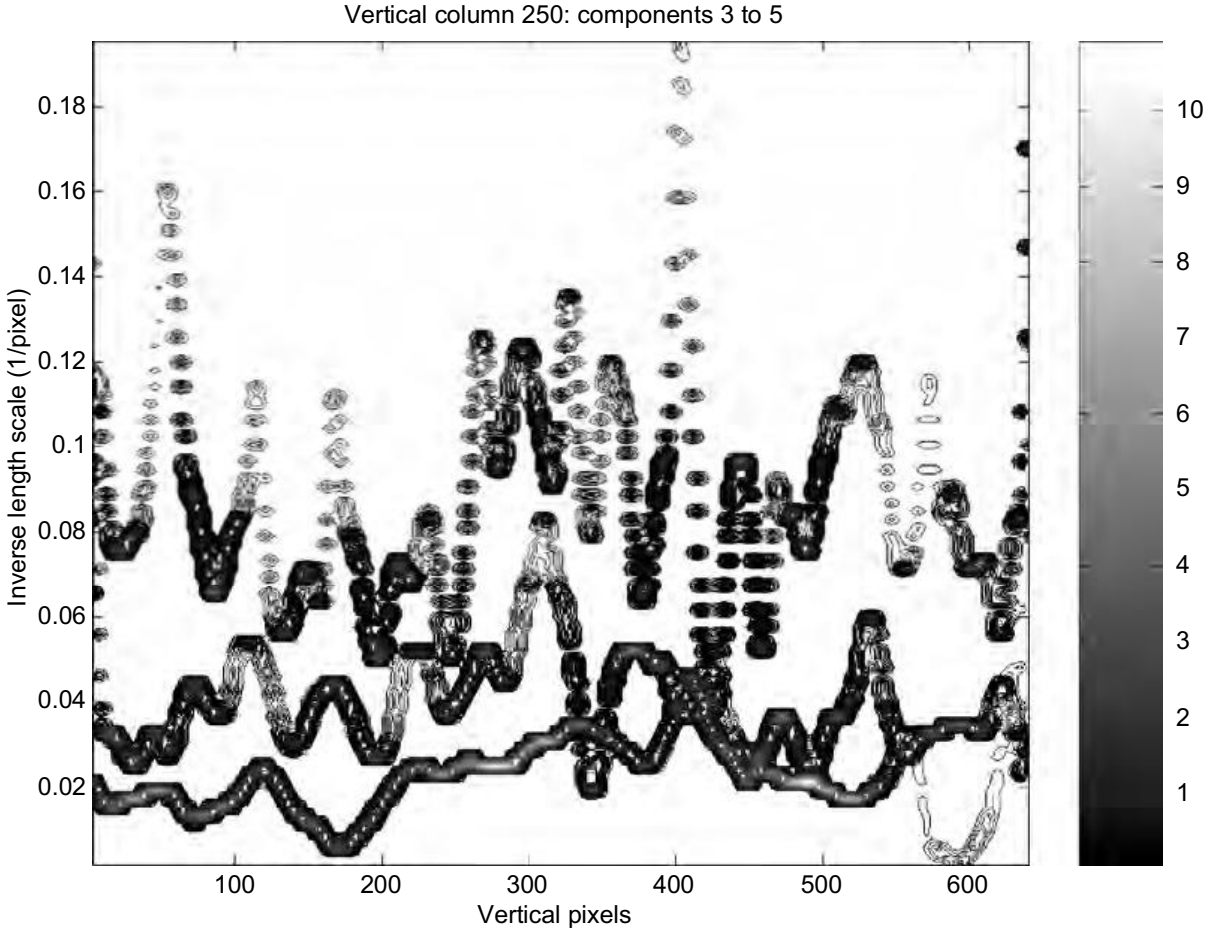

FIGURE 1.19
The contour plot developed from the vertical slice at column 250, using the components 3 to 5. The larger IR values can be seen at longer length scales.

time. Once complete, this two-dimensional array can be split into slices along the time axis. Each of these time slices, representing the variation in data values with time at a single-pixel location, can then be processed with the new NEMD/NHT technique. An example of this can also be seen in Ref. [21]. The NEMD/NHT techniques can thus reveal variations in frequency or time in the data at a specific location in the image sequence.

1.4 Conclusion

With the introduction of the normalization procedure, one of the major obstacles for NEMD/NHT analysis has been removed. Together with the establishment of the confidence limit [6] through the variation of stoppage criterion, and the statistically significant test of the information content for IMF [10,22], and the further development of the concept of IF [23], the new analysis approach has indeed approached maturity for applications empirically, if not mathematically (for a recent overview of developments, see Ref. [24]). The new NEMD/NHT methods provide the best overall approach to determine the IF for nonlinear and nonstationary data. Thus, a new tool is available to aid in further understanding and gaining deeper insight into the wealth of data now possible by remote

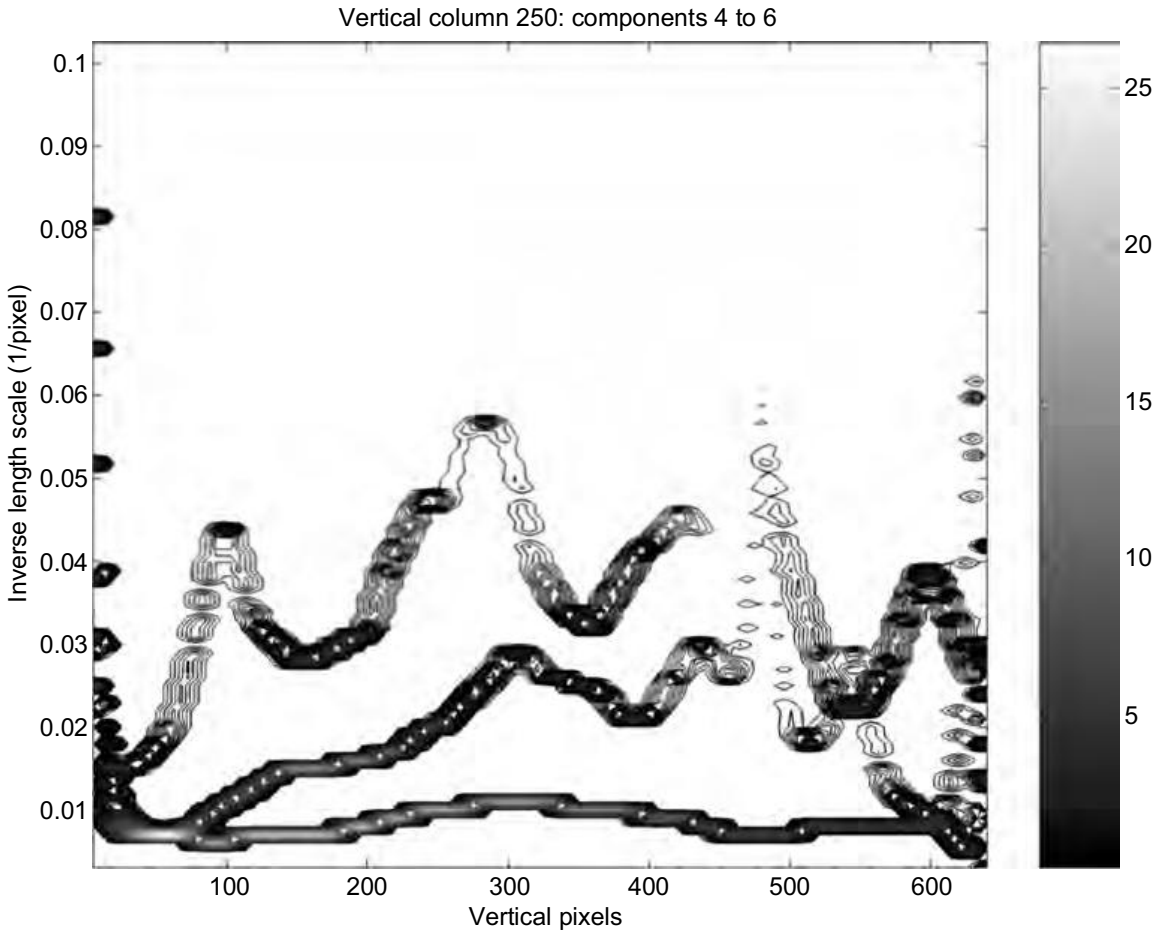

FIGURE 1.20
The contour plot developed from the vertical slice at column 250, using the components 4 through 6, as in Figure 1.19.

sensing and other means. Specifically, the application of the new method to data images was demonstrated.

This new approach is covered by several U.S. Patents held by NASA, as discussed by Huang and Long [25]. Further information on obtaining the software can be found at the NASA authorized commercial site: http://www.fuentek.com/technologies/hht.htm

Acknowledgment

The authors wish to express their continuing gratitude and thanks to Dr. Eric Lindstrom of NASA headquarters for his encouragement and support of the work.

References

1. Huang, N.E., Shen, Z., Long, S.R., Wu, M.C., Shih, S.H., Zheng, Q., Tung, C.C., and Liu, H.H., The empirical mode decomposition method and the Hilbert spectrum for non-stationary time series analysis, *Proc. Roy. Soc. London*, A454, 903–995, 1998.

2. Huang, N.E., Shen, Z., and Long, S.R., A new view of water waves—the Hilbert spectrum, *Ann. Rev. Fluid Mech.*, 31, 417–457, 1999.
3. Flandrin, P., *Time–Frequency/Time–Scale Analysis*, Academic Press, San Diego, 1999.
4. Bedrosian, E., On the quadrature approximation to the Hilbert transform of modulated signals, *Proc. IEEE*, 51, 868–869, 1963.
5. Nuttall, A.H., On the quadrature approximation to the Hilbert transform of modulated signals, *Proc. IEEE*, 54, 1458–1459, 1966.
6. Huang, N.E., Wu, M.L., Long, S.R., Shen, S.S.P., Qu, W.D., Gloersen, P., and Fan, K.L., A confidence limit for the empirical mode decomposition and the Hilbert spectral analysis, *Proc. Roy. Soc. London*, A459, 2317–2345, 2003.
7. Gabor, D., Theory of communication, *J. IEEE*, 93, 426–457, 1946.
8. Huang, N.E., Long, S.R., and Shen, Z., The mechanism for frequency downshift in nonlinear wave evolution, *Adv. Appl. Mech.*, 32, 59–111, 1996.
9. Olhede, S. and Walden, A.T., The Hilbert spectrum via wavelet projections, *Proc. Roy. Soc. London*, A460, 955–975, 2004.
10. Flandrin, P., Rilling, G., and Gonçalves, P., Empirical mode decomposition as a filterbank, *IEEE Signal Proc. Lett.*, 11(2), 112–114, 2004.
11. Castleman, K.R., *Digital Image Processing*, Prentice-Hall, Englewood Cliffs, NJ, 1996.
12. Russ, J.C., *The Image Processing Handbook*, 4th Edition, CRC Press, Boca Raton, 2002.
13. Nunes, J.C., Guyot, S., and Deléchelle, E., Texture analysis based on local analysis of the bidimensional empirical mode decomposition, *Mach. Vision Appl.*, 16(3), 177–188, 2005.
14. Linderhed, A., Compression by image empirical mode decomposition, *IEEE Int. Conf. Image Process.*, 1, 553–556, 2005.
15. Linderhed, A., Variable sampling of the empirical mode decomposition of two-dimensional signals, *Int. J. Wavelets, Multi-resolut. Inform. Process.*, 3, 2005.
16. Linderhed, A., 2D empirical mode decompositions in the spirit of image compression, *Wavelet Independ. Compon. Analy. Appl. IX*, *SPIE Proc.*, 4738, 1–8, 2002.
17. Long, S.R., NASA Wallops Flight Facility Air–Sea Interaction Research Facility, *NASA Reference Publication*, No. 1277, 1992, 29 pp.
18. Long, S.R., Lai, R.J., Huang, N.E., and Spedding, G.R., Blocking and trapping of waves in an inhomogeneous flow, *Dynam. Atmos. Oceans*, 20, 79–106, 1993.
19. Long, S.R., Huang, N.E., Tung, C.C., Wu, M.-L.C., Lin, R.-Q., Mollo-Christensen, E., and Yuan, Y., The Hilbert techniques: An alternate approach for non-steady time series analysis, *IEEE GRSS*, 3, 6–11, 1995.
20. Long, S.R. and Klinke, J., A closer look at short waves generated by wave interactions with adverse currents, *Gas Transfer at Water Surfaces*, Geophysical Monograph 127, American Geophysical Union, 121–128, 2002.
21. Long, S.R., Applications of HHT in image analysis, *Hilbert–Huang Transform and Its Applications*, Interdisciplinary Mathematical Sciences, 5, 289–305, World Scientific, Singapore, 2005.
22. Wu, Z. and Huang, N.E., A study of the characteristics of white noise using the empirical mode decomposition method, *Proc. Roy. Soc. London*, A460, 1597–1611, 2004.
23. Huang, N.E., Wu, Z., Long, S.R., Arnold, K.C., Blank, K., and Liu, T.W., On instantaneous frequency, *Proc. Roy. Soc. London* 2006, in press.
24. Huang, N.E., Introduction to the Hilbert–Huang transform and its related mathematical problems, *Hilbert–Huang Transform and Its Applications*, Interdisciplinary Mathematical Sciences, 5, 1–26, World Scientific, Singapore, 2005.
25. Huang, N.E. and Long, S.R., A generalized zero-crossing for local frequency determination, US Patent pending, 2003.